ACS APPLIED MATERIALS & INTERFACES

Research Article

www.acsami.org

Negative Electro-conductance in Suspended 2D WS_2 Nanoscale Devices

Ye Fan,[†] Alex W. Robertson,[†] Xiaowei Zhang,[‡] Martin Tweedie,[†] Yingqiu Zhou,[†] Mark H. Rummeli,[§,∥,⊥] Haimei Zheng,[‡] and Jamie H. Warner*[,†]

[†]Department of Materials, University of Oxford, Parks Rd, Oxford, OX1 3PH, United Kingdom

[‡]Materials Sciences Division, Lawrence Berkeley National Laboratory, Berkeley, California 94720, United States

[§]IFW Dresden, P.O. Box D-01171 Dresden, Germany

[∥]College of Physics, Optoelectronics and Energy & Collaborative Innovation Center of Suzhou Nano Science and Technology, Soochow University, Suzhou 215006, China

[⊥]Centre of Polymer and Carbon Materials, Polish Academy of Sciences, M. Curie-Sklodowskiej 34, Zabrze 41-819, Poland

Supporting Information

ABSTRACT: We study the *in situ* electro-conductance in nanoscale electronic devices composed of suspended monolayer WS_2 with metal electrodes inside an aberration-corrected transmission electron microscope. Monitoring the conductance changes when the device is exposed to the electron beam of 80 keV energy reveals a reversible decrease in conductivity with increasing beam current density. The response time of the electro-conductance when exposed to the electron beam is substantially faster than the recovery time when the beam is turned off. We propose a charge trap model that accounts for excitation of electrons into the conduction band and localized trap states from energy supplied by inelastic scattering of incident 80 keV electrons. These results show how monolayer transition metal dichalcogenide 2D semiconductors can be used as transparent direct electron detectors in ultrathin nanoscale devices.

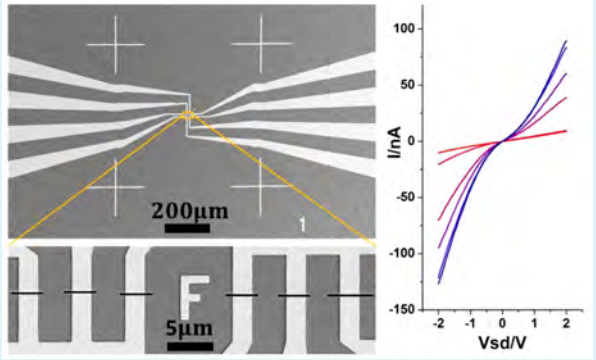

KEYWORDS: *electro-conductance, WS_2, 2D, in situ, TEM*

INTRODUCTION

2D semiconductors, such as WS_2 and MoS_2, have recently attracted significant attention due to their direct band gap, which makes them suitable for semiconductor electronic and optoelectronic applications including transistors, photodetectors, and light-emitting devices.[1] The ultrathin monolayer has enabled a variety of different device structures to be explored, including lateral and vertical geometries. Electronic applications from diodes with homojunctions and heterojunctions,[2,3] to transistors and logic circuits have been reported.[4−6] Photodetectors making use of the photoconductivity of single material or photoinduced current in pn junctions have also been realized.[7,8] The former device generally exhibits a large photoresponsivity but slow response time due to the existence of trapped states.[9−11]

Despite the intensive work on 2D photodetectors, investigations on electron detection using 2D materials is limited. Part of the reason is the challenge of experimentally implementing electron irradiation compared to optical excitation of devices. *In situ* electrical measurements of devices inside a transmission electron microscope (TEM) using specialized electrical biasing holders enable simultaneous characterization of electrical performance and atomic structure. Recent works on nanowires have made use of STEM:TEM *in situ* TEM holders that utilize piezo controlled sharp metal tips as electrodes to direct contact suspended wires,[12,13] but this approach is not ideal for making uniform contacts with 2D materials that have a larger surface area as compared to nanowires. Electron beam lithography to pattern and fabricate nanoscale electronic devices containing graphene has proved to be a more effective approach to achieve *in situ* electrical measurement of 2D materials. The conductivity change of graphene as a nanoribbon, or as an atomic carbon chain, has been studied by different groups.[14−18] A Schottky junction between graphene nanoribbons and a bulk region has also been reported.[19] When graphene is placed under high electrical bias, crack propagation has been shown to occur.[20] More advanced lithographic methods have shown that *in situ* gating of graphene nanoribbons can be achieved using side gates within *in situ* TEM experiments.[21] More recently, the *in situ* electrical biasing

Received: September 10, 2016
Accepted: November 16, 2016
Published: November 23, 2016

DOI: 10.1021/acsami.6b11480
ACS Appl. Mater. Interfaces 2016, 8, 32963−32970

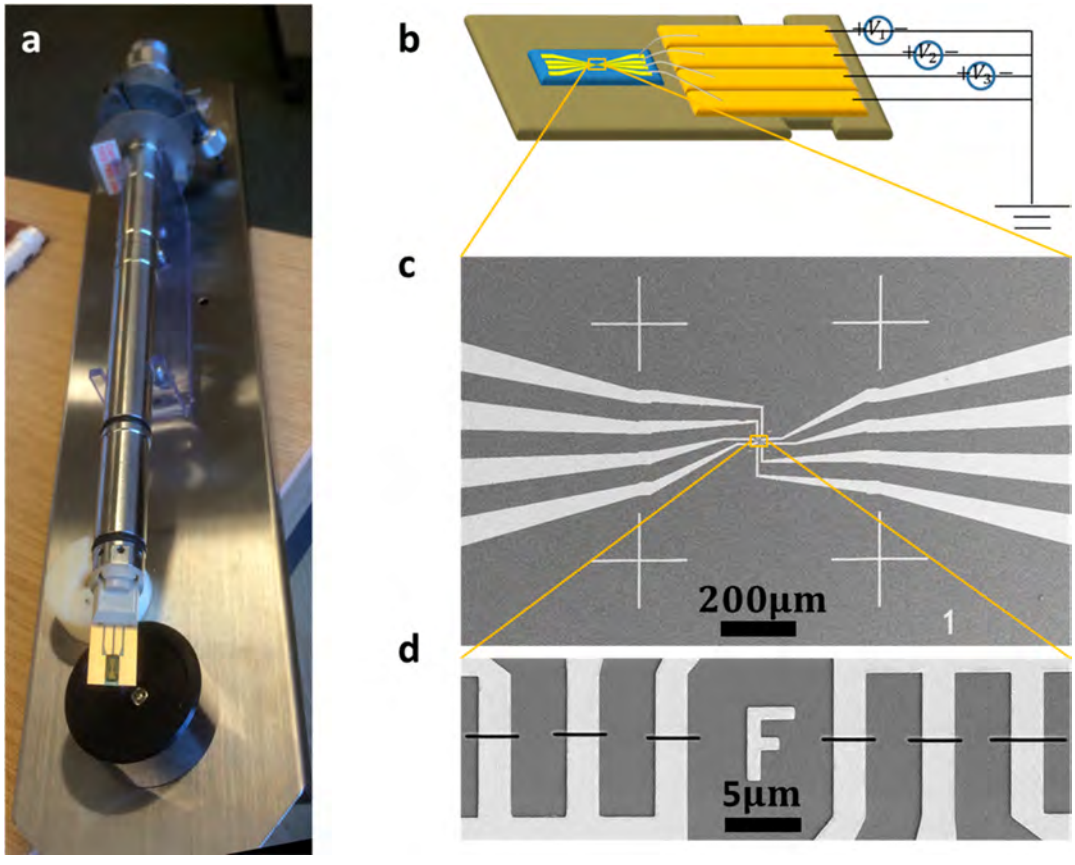

Figure 1. Experimental setup of *in situ* electrical biasing within the AC-TEM. (a) Photograph of the electrical *in situ* biasing TEM holder. (b) Schematic image of the nanoscale electronic devices with bond pads to connect to the biasing holder with electrical feedthroughs. (c, d) SEM images of the electrodes on the chip. Electrodes are produced on the silicon nitride (SiN) insulating layer covering the silicon substrate for *in situ* electrical measurement.

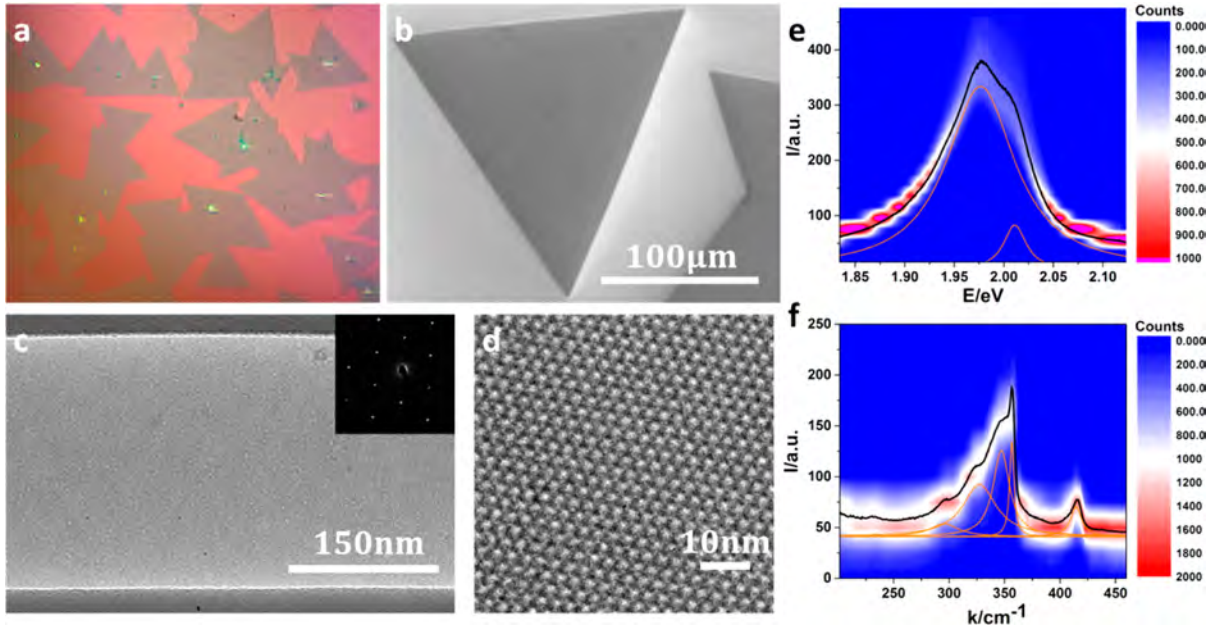

Figure 2. Characterization of CVD WS_2. (a) Optical microscope image of as-grown WS_2 on a silicon substrate. (b) SEM image of a WS_2 domain. (c) Low-magnification TEM image of suspended WS_2 within the *in situ* TEM electrical holder. Inset is the electron diffraction pattern of WS_2. (d) AC-TEM image of the hexagonal WS_2 lattice with black atom contrast. (e) Histogram of PL spectra from WS_2. The black curve is the average spectrum of WS_2 over all spots. Orange curves are the trion and exciton peaks that comprise the PL spectrum. (f) Histogram of Raman spectra from WS_2. The black line is the average spectrum of WS_2 over all spots in the statistic. Orange curves are phonon modes that contribute to the Raman spectrum.

DOI: 10.1021/acsami.6b11480
ACS Appl. Mater. Interfaces 2016, 8, 32963−32970

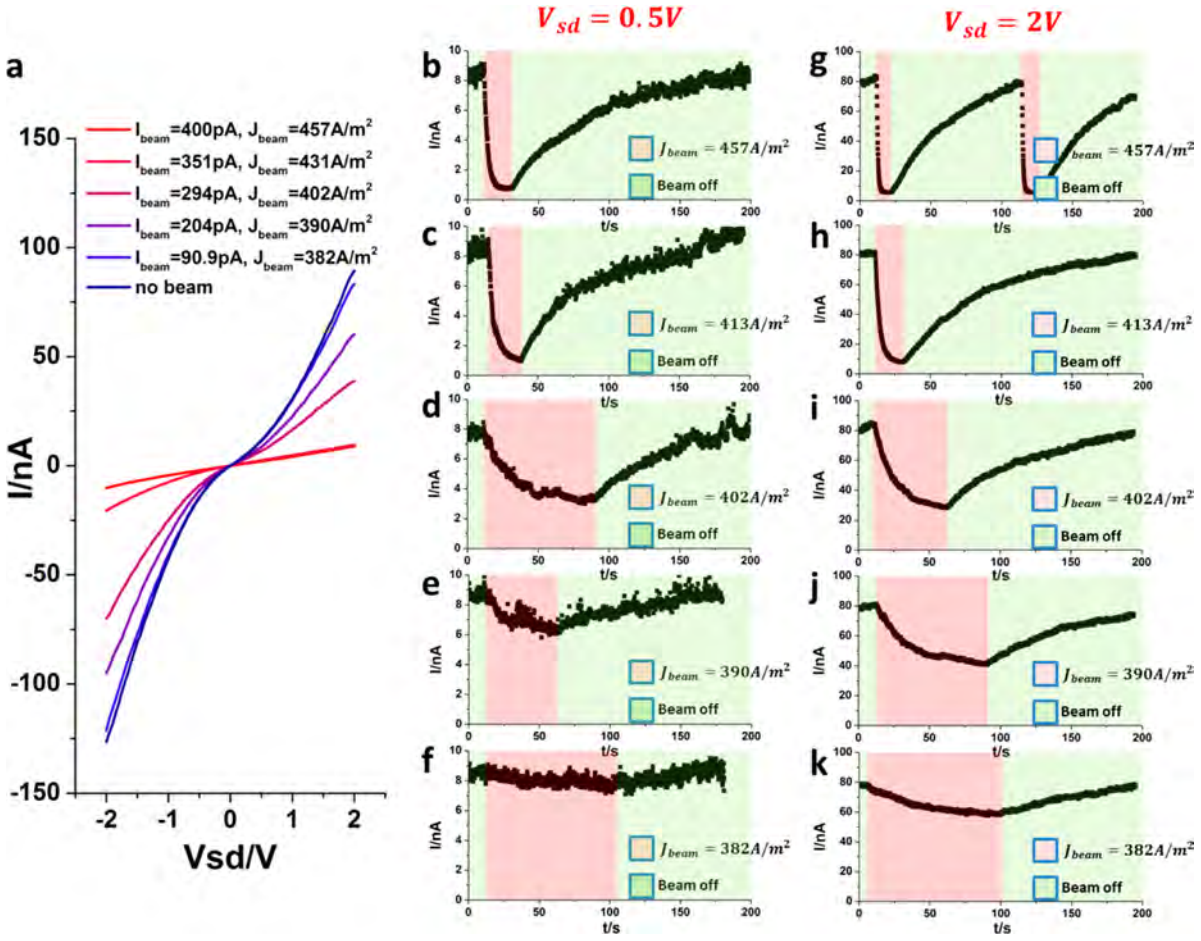

Figure 3. Current response of WS_2 to incident electron beam exposure. (a) IV sweep under different electron illumination conditions. Nonlinear IV curve is typical for WS_2 devices with a Schottky contact. DC current decreases with increasing electron beam intensity (I_{beam}) and density (J_{beam}). (b–f) Time-resolved response of device to incident electron beam at low bias (V_{sd} = 0.5V). The on/off state of the incident electron beam is indicated by the color of the background (green background for beam off, red background for beam on). (g–k) Time-resolved response of device to incident electron beam at high bias (V_{sd} = 2V). The on/off state of the incident electron beam is indicated by the color of the background (green background for beam off, red background for beam on).

TEM studies of 2D materials has been extended from graphene to MoS_2, where conductivity changes induced by electron beam damage was reported.[22]

The atomically thin nature of 2D semiconductors (e.g., WS_2) makes them interesting candidates for applications in electron detection. In electron detectors made with 3D bulk materials, nearly all the incident electrons are stopped by the detector, making the detector opaque and the mechanisms behind the electro-conductance response relatively complex. 2D materials such as WS_2 are highly transparent to an electron beam due to their monolayer thickness and thus offer the opportunity for electron detectors that are effectively electron transparent, enabling the majority of the electron beam to propagate through the device and proceed to other multifunctional detectors.

In this report, we examine the electron detection ability of suspended monolayer WS_2 nanoelectronic devices using an *in situ* electrical biasing holder within an aberration-corrected TEM (AC-TEM). An accelerating voltage of 80 kV is used to provide electrons with reduced knock-on damage, and therefore, holes or damage will not rapidly occur in the ultrathin WS_2 monolayer. Changes in conductivity of WS_2 as a function of electron beam current density are studied, along with switching of the electron beam on and off to demonstrate nondestructive cycling of the electro-conductance.

We fabricated nanoelectronic devices using electron beam lithography methods on a thin silicon chip with 100 nm silicon nitride (SiN) thin film. Gold electrodes are aligned to a 10 μm × 50 μm suspended SiN observation window in the center of the chip. The slits in the electrodes are produced using focused ion beam (FIB) irradiation, using similar methods as we previously reported.[23] The introduction of the slit in the gold wire separates the source from the drain to produce a two-electrode structure. Six devices in total are fabricated on one chip and are categorized into two groups. Devices in the same group are co-sourced (Figure 1d). The SEM images of the as-fabricated chip are shown in Figure 1c,d. The channel length of our device is 250 nm, with a 2 μm channel width. The large aspect ratio between channel width and length provides a uniform electrical field through the channel material (WS_2) and guarantees that most of the current flows directly through the WS_2 between the electrodes when biased. Details are described in the Supporting Information.

RESULTS AND DISCUSSION

We characterized the chemical vapor deposition (CVD) grown WS_2 before carrying out *in situ* electrical measurements to

DOI: 10.1021/acsami.6b11480
ACS Appl. Mater. Interfaces 2016, 8, 32963–32970

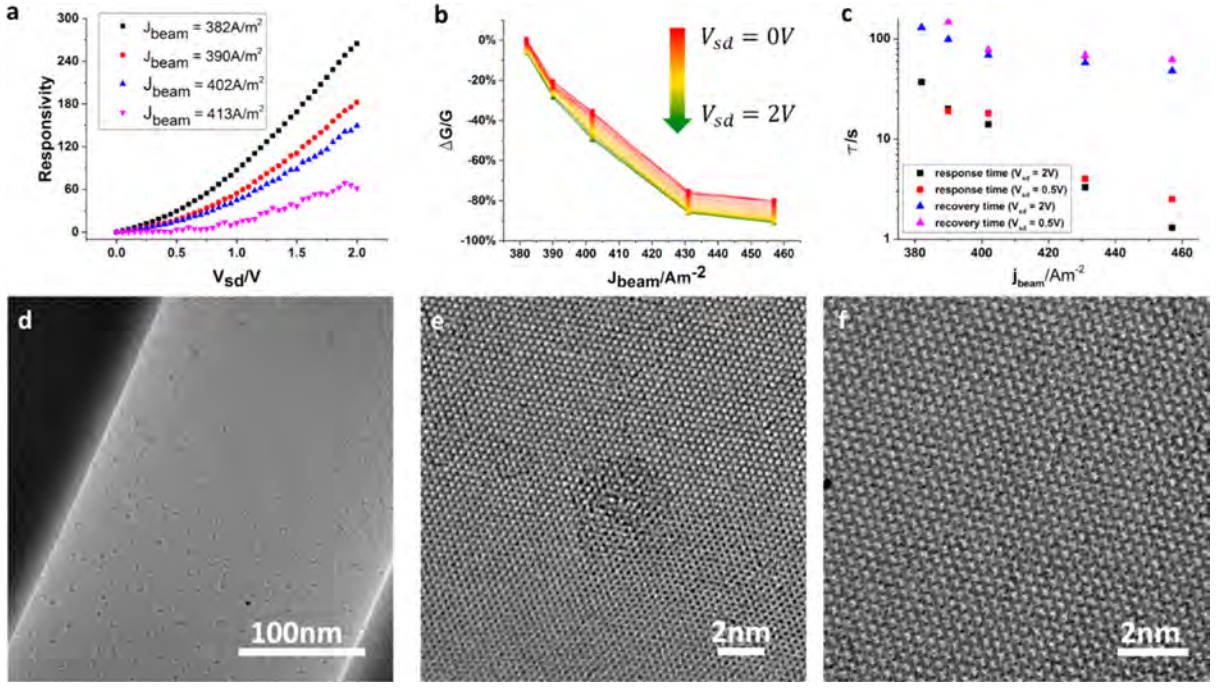

Figure 4. Characterization of the device to incident electron beam. (a) Electro-responsivity of the WS_2 device. The electro-responsivity is defined as the ratio between change of IV current and incident electron beam, which increases with increasing source−drain bias as well as incident beam current. (b) Relative change in conductance of the device due to incident electron beam. The conductivity of WS_2 decreases down to 10% of its original value when illuminated by the electron beam. (c) Dependence of response time on incident beam density. Both the response and recovery times do not strongly rely on the source−drain bias. The response time decreases with increasing beam density, while the recovery time keeps almost unanged. (d−f) TEM images of WS_2 in this experiment. (d) Low-magnification TEM image of WS_2. Small clusters appear on the WS_2 after Joule annealing. (e) AC-TEM image of one cluster on WS_2 lattice. (f) AC-TEM image of clean region of WS_2.

ensure its quality. Single crystal domains of CVD grown WS_2 (Figure 2a,b) are used for the *in situ* measurement in this study. The low-magnification TEM image in Figure 2c shows the WS_2 after transfer onto the *in situ* TEM chip and reveals the suspended region. Selected area electron diffraction was taken from this suspended region of WS_2 and shows only one set of electron diffraction spots, confirming the single crystallinity of WS_2 across the electrode gap (inset of Figure 2c). Despite the small amount of amorphous residue on the surface, the transferred WS_2 is clean enough to resolve the atomic lattice in AC-TEM images (Figure 2d). We find that, if the WS_2 contains excessive amounts of surface contamination, then the measurement of the electro-conductance becomes unstable. The quality of WS_2 used in this experiment is further evaluated by photoluminescence and Raman spectroscopy. Since only a small portion of WS_2 is across the device, we take hundreds of different measurement spots to get statistical information on overall quality of WS_2 in this experiment. Panels (e) and (f) in Figure 2 are the histograms of spectra of CVD grown WS_2. In each image, the color reflects the counts and the black curve marks the average spectrum. Both photoluminescence (PL) and Raman spectra are measured with a 532 nm laser. The PL spectrum consists of a trion peak and an exciton peak. The energy of the trion and exciton is measured as 1.98 and 2.01 eV, respectively, which is in accordance with previously reported values.[24,25] The CVD grown WS_2 used in our work is n-doped according to our previous measurements,[45] similar to other reports.[24,25] The doping is likely to arise from either S vacancies, oxidization, surface adsorbates, or substitutional impurities. Many secondary resonance peaks appear in the Raman spectrum of our sample, similar to previously reported works.[26,27] The peak shift and height ratio between the E_{2g} (356.5 cm^{-1}) peak and the A_{1g} (414.4 cm^{-1}) peak are 57.9 cm^{-1} and 3.16, respectively. This confirms the single layer nature of the CVD WS_2.[28]

Figure 3 shows the change in current of the biased WS_2 device upon exposure to the electron beam. The monolayer single crystal CVD grown WS_2 in our experiment exhibits a negative electro-conductivity; i.e., the conductance of WS_2 is lowered by the incident electron beam. By varying the incident electron beam density, we measure a change in the IV curve of WS_2. It should be noted that, due to the nonuniformity of the electron beam, especially when the beam size is comparable to the size of the slot covered by WS_2, the total current is not linearly dependent on the beam density. Before carrying out the electro-conductivity measurements, the device is annealed by Joule heating. Similar to previous reports on electronic measurement of WS_2,[29] we find that a long period of Joule annealing is necessary to get stable device performance. Inspection of the device by high-resolution TEM imaging confirms that this procedure does not damage the WS_2. Although this cannot fully rule out defects caused by Joule annealing, the effect of newly created defects by the annealing is expected not to be significant. The IV sweep of WS_2 under different electron beam current densities is shown in Figure 3a. When the electron beam is off, "dark" current up to ∼100 nA is measured under 2 V bias. This results in a conductivity of 6.1 nS (by assuming channel length = 250 nm, channel width = 2000 nm), which is typical for single layer WS_2 in vacuum.[29−31] The nonlinear IV curve is due to the Schottky contact between WS_2 and the gold electrode contact. When the electron beam is switched on and is incident onto the WS_2 device, the DC

DOI: 10.1021/acsami.6b11480
ACS Appl. Mater. Interfaces 2016, 8, 32963−32970

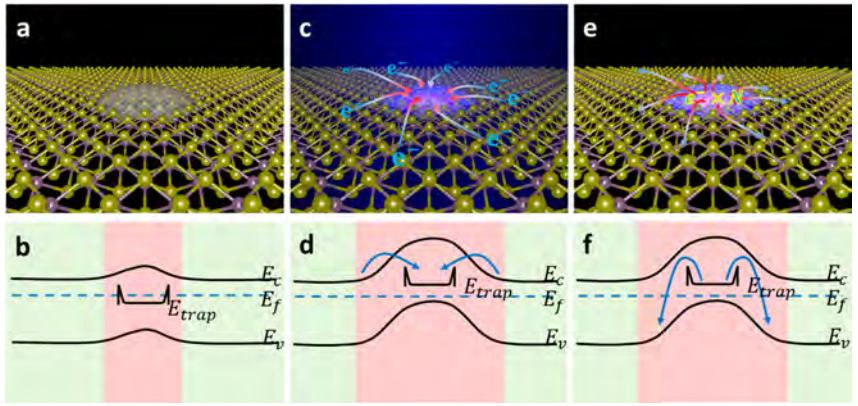

Figure 5. Schematic illustrating the mechanism of negative electro-conductance in suspended WS_2. (a) Artistic image and (b) band diagram of WS_2 with trapped center before e-beam illumination. (c) Artistic image and (d) band diagram of WS_2 with trapped center being illuminated by incident electron beam. Hot charge carriers (electrons) fill the trapped states quickly. (e) Artistic image and (f) band diagram of WS_2 with trapped center right after the incident beam is shut off. The trapped center slowly discharges.

current drops down to less than 10% of the dark current. For example, the current passing through WS_2 at a 2 V bias decreases from 90 to 8.7 nA when the beam current density increases from 0 to 457 A/m^2 (Figure 3a).

An intriguing response and recovery process of WS_2 to incident electron beam is revealed in Figures 3b–f and 3g–k. DC current flow in WS_2 decreases sharply when the device is exposed to the electron beam, but increases slowly after the beam is shut off. Hereafter, we call the decreasing of DC current when turning on the electron beam as the "response" process and the increasing of DC current due to turning off the electron beam as the "recovery" process. The cyclic response and recovery processes are measured multiple times by manually controlling the beam valve to switch the electron beam on and off. One cycle of each measurement is shown in Figure 3 to illustrate the behavior. The current recovers to its original value when the beam is turned off again (as seen in Figure 3b–g).

To further understand the DC response of WS_2 to the incident electron beam, we define the electro-responsivity as following

$$\text{Responsivity} = \left| \frac{I - I_{\text{dark}}}{I_{\text{beam}}} \right|$$

where I is the measured source–drain current when the electron beam illuminates the device, I_{dark} is the dark current (i.e., the current of the device when the electron beam is off), and I_{beam} is the incident beam current. The electro-responsivity defined here can be seen as an analogy to the photoresponsivity and represents how sensitive the device is to the incident electron beam. The electro-responsivity at each bias and electron beam density is calculated and shown in Figure 4a. Within our experimental range, the electro-responsivity increases monotonically with increasing bias and incident beam current.

The dependence of electro-responsivity on source–drain bias indicates that our device acts as an "electro-conductor", analogous to a photoconductor, of which conductance changes when exposed to light. The change of conductance is plotted in Figure 4b. The conductance of the device varies for different source–drain biases due to its Schottky contact with the gold electrodes. However, the trend of decreasing conductance with increasing beam density is clear (Figure 4b). When the beam current density reaches 457 A/m^2, the conductance of WS_2 decays to only 9.8% of its conductance in the dark.

Besides the change in conductance, the reaction speed of WS_2 to the external electron beam is also studied. Two factors prohibit us from further increasing the electron beam intensity: First, the electron-beam-induced damage to WS_2 becomes significant with higher electron beam density. Additionally, the uniformity of the electron beam becomes nonperfect, which increases the measurement error. By fitting a time dependence curve in Figure 3b,c, with a formula describing an exponential decay

$$I = I_0 + I_1 \exp(-t/\tau)$$

where I is the measured current, I_0 and I_1 are two fitting parameters, and τ is the characteristic response time of the device, we can extract the response (or recovery) time of our device (Figure 4c). Both the response time and the recovery time are found to be independent of source–drain bias. However, the response time varied from the range of 10^0 to 10^1 s in our experiment, while the recovery time is stable at around 10^2 s. The response time is about 1 order of magnitude smaller than the recovery time (Figure 4c), which means the device reacts much quicker to the turning on of the electron beam compared to turning off. The time scale of response and recovery is similar to TMD high-gain photodetectors using CVD grown material,[7,32] but slower than most photodetectors.[4,33] The recovery time is almost constant regardless of the density of the beam illumination on the device. On the contrary, the response time significantly depends on the beam density.

Although negative electro-conductance is rarely reported, there are several mechanisms that could help to understand the experimental results. We start by considering the electron-beam-induced damage, which is found to alter the conductivity in graphene and MoS_2.[46,47] It is known that electron beam damage to WS_2 can introduce sulfur vacancies and other defects.[34,35] Some of the vacancies recombine into line defects at high temperature, which can serve as a 1D conductive channel when infinitely long.[36] We do find small holes and vacancies after long periods of electron beam radiation, which is similar to references as mentioned. However, no line defects were observed during the experiment (Figure 4e,f), though Joule heating effect may increase the temperature of the device. Besides, all IV measurements are repeated by several cycles to

DOI: 10.1021/acsami.6b11480
ACS Appl. Mater. Interfaces 2016, 8, 32963–32970

rule out the possibility that beam damage dominates the changes in conductance as we observed. In this way, it is unlikely that our observation is due to structure change.

Another possible explanation for negative electro-conductance is the decreasing of charge carrier mobility due to formation of charged electron−hole clusters (like trion) when an abundance of free electrons and holes exist in the system. This mechanism explains the transient negative photo-conductivity in monolayer MoS_2 at low temperature.[37] However, our experiment is different in both measurement time scale (second vs picosecond) and temperature (room temperature vs cryogenic temperature). In this way, formation of electron−hole combinations is unlikely to account for our experiment results.

One mechanism that may explain the negative electro-conductance of WS_2 is the trapping of hot charge carriers. A similar mechanism is widely used to explain the negative photoconductance phenomenon.[38−40] The 80 keV electron beam energy in our experiment is much higher than the band gap of WS_2 (~2 eV). Inelastic scattering leads to the transfer of energy from the electron beam to the WS_2 that can cause a large number of electrons to be promoted to the conduction band as hot charge carriers. Previous studies reveal that structural defects,[41,42] surface nanoclusters,[39,43] or even absorbed molecules[44] can act as charge traps for electrons in the conduction band. This will result in a negatively charged trap center surrounded by a positively charged local region of the WS_2. These negatively charged trap centers may scatter the charge carriers in WS_2. Another way to view the process is to consider the charged trap centers as a local negative gate bias applied to WS_2, which results in a p-doping of the originally n-doped WS_2. A lot of small p−n junctions may then be formed inside the WS_2 sheet and thus reduce the conductivity. This mechanism is schematically illustrated in Figure 5.

Our experimental results fit well with the process discussed above. According to this mechanism, when increasing the incident beam density, the trapped states should be charged more quickly. In our experiment, the response time negatively depends on the incident electron beam density (Figure 4c), which is as expected. On the other hand, the time to discharge the trap (recovery time) should not rely on beam current density that the device is previously exposed to, but only on the energy barrier between the trap centers and WS_2. In addition, hot electrons stimulated by the incident electron beam can easily overcome the energy barrier around the traps and lead to a quick response time (Figure 5c,d). When the traps are discharged, trapped electrons can only slowly tunnel through the barrier and thus the recovery time is much slower than the response time (Figure 5e,f). All of these phenomena are supported by our experiments (Figure 4c). The electron response in Figure 3 is actually measured for several cycles, shown in the Supporting Information. Both the response and recovery times are unchanged during the measurement, and thus the density of trapped states is unlikely to change significantly.

CONCLUSION

In situ nanoscale electronic devices containing suspended monolayer WS_2 are demonstrated to exhibit negative electro-conductivity. The conductance of the WS_2 is tuned by external electron beam exposure up to an order of magnitude. The response of the device to an external electron beam is found to be of the time scale of seconds, which is slower than the state-of-art electron detectors, which have frequencies around 100 frames per second.[48] Further studies on improving the electron detection speed would be beneficial. These fundamental results may help the future development of transparent ultrathin direct electron beam detectors based on 2D transition metal dichalcogenides.

METHODS

Fabrication of the Chip. Si wafers (P-doped, 200 μm in thickness and 4 in. in diameter) are cleaned through an RCA standard cleaning process. The Si-rich silicon nitride (SiN) thin film (100 nm in thickness) is then deposited on both sides of the cleaned Si wafers by the low-pressure chemical vapor deposition (LPCVD) method. During the deposition process, substrate temperature is fixed at 850 °C and the reaction gas ratio between SiH_2Cl_2 and NH_3 is kept at 100:25. The observation window is patterned by photolithography on one side of the SiN film, then etched away by reactive ion etching. Subsequently, silicon inside of the observation window is etched by wet etching (45% w/w KOH as the etching solution at 80 °C), leaving suspended SiN covering on the observation window.

Fabrication of the Device. The chip for *in situ* electrical measurement is patterned by e-beam lithography (EBL), followed by the metallization and lift-off process. The electrode is aligned to the observation window in the suspended silicon nitride thin film by direct imaging with SEM inside of the EBL facility. 90 nm Au is thermally evaporated onto the chip with a 10 nm Cr adhesion layer. The electrodes are then cut by focused ion beam (FIB) to separate the source from the drain. All three devices on one side are cogrounded in the measurements. WS_2 is transferred onto the device by a PMMA assisted wet transfer method.

Electrical Measurement. Samples prepared on specialized Si TEM chips were mounted onto an *in situ* electrical biasing holder and loaded into the TEM. Electrical measurements are made using a Keithley 2400LV semiconductor measurement unit. The Keithley 2400 SMU has a response time better than 50 μs, which is far below the characteristic time in this experiment. Given this, we do not need to consider the influence of IRF to the measurement results.

Transmission Electron Microscopy. Aberration-corrected TEM was performed using Oxford's JEOL 2200MCO with a CEOS image corrector. Accelerating voltage was set to 80 kV. Beam current density was calibrated by using a Faraday cage to measure total beam current and then imaging the condensed beam to determine its size. This enables the CCD counts to be correlated to electron dose.

ASSOCIATED CONTENT

Supporting Information

The Supporting Information is available free of charge on the ACS Publications website at DOI: 10.1021/acsami.6b11480.

Time-resolved IV measurement of WS_2 (PDF)

AUTHOR INFORMATION

Corresponding Author

*E-mail: Jamie.warner@materials.ox.ac.uk.

ORCID

Jamie H. Warner: 0000-0002-1271-2019

Notes

The authors declare no competing financial interest.

ACKNOWLEDGMENTS

J.H.W. thanks the Royal Society for support. Y.F. is thankful for the support from the Clarendon Scholarship from the University of Oxford. H.Z. is thankful for the support from the DOE Early Career Research Program. M.H.R. thanks the National Natural Science Foundation of China and the

DOI: 10.1021/acsami.6b11480
ACS Appl. Mater. Interfaces 2016, 8, 32963−32970

National Science Centre (OPUS programme, Grant: 015/19/B/ST5/03399).

REFERENCES

(1) Wang, Q. H.; Kalantar-Zadeh, K.; Kis, A.; Coleman, J. N.; Strano, M. S. Electronics and Optoelectronics of Two-Dimensional Transition Metal Dichalcogenides. *Nat. Nanotechnol.* **2012**, *7*, 699−712.

(2) Suh, J.; Park, T. E.; Lin, D. Y.; Fu, D.; Park, J.; Jung, H. J.; Chen, Y.; Ko, C.; Jang, C.; Sun, Y.; Sinclair, R.; Chang, J.; Tongay, S.; Wu, J. Doping against the Native Propensity of MoS2: Degenerate Hole Doping by Cation Substitution. *Nano Lett.* **2014**, *14*, 6976−6982.

(3) Li, M.-Y.; Shi, Y.; Cheng, C.-C.; Lu, L.-S.; Lin, Y.-C.; Tang, H.-L.; Tsai, M.-L.; Chu, C.-W.; Wei, K.-H.; He, J.-H.; Chang, W.-H.; Suenaga, K.; Li, L.-J. Epitaxial Growth of a Monolayer WSe2-MoS2 Lateral P-N Junction with an Atomically Sharp Interface. *Science* **2015**, *349*, 524−528.

(4) Yin, Z.; Li, H.; Li, H.; Jiang, L.; Shi, Y.; Sun, Y.; Lu, G.; Zhang, Q.; Chen, X.; Zhang, H. Single-Layer MoS2 Phototransistors. *ACS Nano* **2012**, *6*, 74−80.

(5) Tosun, M.; Chuang, S.; Fang, H.; Sachid, A. B.; Hettick, M.; Lin, Y.; Zeng, Y.; Javey, A. High-Gain Inverters Based on WSe2 Complementary Field-Effect Transistors. *ACS Nano* **2014**, *8*, 4948−4953.

(6) Wang, H.; Yu, L.; Lee, Y.-H.; Shi, Y.; Hsu, A.; Chin, M. L.; Li, L.-J.; Dubey, M.; Kong, J.; Palacios, T. Integrated Circuits Based on Bilayer MoS2 Transistors. *Nano Lett.* **2012**, *12*, 4674−4680.

(7) Lopez-Sanchez, O.; Lembke, D.; Kayci, M.; Radenovic, A.; Kis, A. Ultrasensitive Photodetectors Based on Monolayer MoS2. *Nat. Nanotechnol.* **2013**, *8*, 497−501.

(8) Pospischil, A.; Furchi, M. M.; Mueller, T. Solar-Energy Conversion and Light Emission in an Atomic Monolayer P-N Diode. *Nat. Nanotechnol.* **2014**, *9*, 257−261.

(9) Koppens, F. H. L.; Mueller, T.; Avouris, P.; Ferrari, A. C.; Vitiello, M. S.; Polini, M. Photodetectors Based on Graphene, Other Two-Dimensional Materials and Hybrid Systems. *Nat. Nanotechnol.* **2014**, *9*, 780−793.

(10) Kufer, D.; Konstantatos, G. Highly Sensitive, Encapsulated MoS2 Photodetector with Gate Controllable Gain and Speed. *Nano Lett.* **2015**, *15*, 7307−7313.

(11) Fan, Y.; Zhou, Y.; Wang, X.; Tan, H.; Rong, Y.; Warner, J. H. Photoinduced Schottky Barrier Lowering in 2D Monolayer WS 2 Photodetectors. *Adv. Opt. Mater.* **2016**, *4*, 1573−1581.

(12) Wang, Z. L.; Poncharal, P.; de Heer, W. A. Nanomeasurements of Individual Carbon Nanotubes by in Situ TEM. *Pure Appl. Chem.* **2000**, *72*, 209−219.

(13) Jin, C.; Wang, J.; Wang, M.; Su, J.; Peng, L.-M. In-Situ Studies of Electron Field Emission of Single Carbon Nanotubes inside the TEM. *Carbon* **2005**, *43*, 1026−1031.

(14) Qi, Z. J.; Rodríguez-Manzo, J. A.; Hong, S. J.; Park, Y. W.; Stach, E. A.; Drndić, M.; Johnson, A. T. C. Direct Electron Beam Patterning of Sub-5nm Monolayer Graphene Interconnects. *Proc. SPIE* **2013**, *8680*, 86802F.

(15) Qi, Z. J.; Rodríguez-Manzo, J. a.; Botello-Méndez, A. R.; Hong, S. J.; Stach, E. a.; Park, Y. W.; Charlier, J.-C.; Drndić, M.; Johnson, A. T. C. Correlating Atomic Structure and Transport in Suspended Graphene Nanoribbons. *Nano Lett.* **2014**, *14*, 4238−4244.

(16) Qi, Z. J.; Daniels, C.; Hong, S. J.; Park, Y. W.; Meunier, V.; Drndic, M.; Johnson, A. T. C. Electronic Transport of Recrystallied Freesanding Graphene Nanoribbons. *ACS Nano* **2015**, *9*, 3510−3520.

(17) Lu, Y.; Merchant, C. A.; Drndić, M.; Johnson, A. T. C. In Situ Electronic Characterization of Graphene Nanoconstrictions Fabricated in a Transmission Electron Microscope. *Nano Lett.* **2011**, *11*, 5184−5188.

(18) Cretu, O.; Botello-Mendez, A. R.; Janowska, I.; Pham-Huu, C.; Charlier, J. C.; Banhart, F. Electrical Transport Measured in Atomic Carbon Chains. *Nano Lett.* **2013**, *13*, 3487−3493.

(19) Wang, Q.; Kitaura, R.; Suzuki, S.; Miyauchi, Y.; Matsuda, K.; Yamamoto, Y.; Arai, S.; Shinohara, H. Fabrication and In Situ Transmission Electron Microscope Characterization of Free-Standing Graphene Nanoribbon Devices. *ACS Nano* **2016**, *10*, 1475−1480.

(20) Barreiro, A.; Börrnert, F.; Rümmeli, M. H.; Büchner, B.; Vandersypen, L. M. K. Graphene at High Bias: Cracking, Layer by Layer Sublimation, and Fusing. *Nano Lett.* **2012**, *12*, 1873−1878.

(21) Rodríguez-Manzo, J. A.; Qi, Z. J.; Crook, A.; Ahn, J.; Johnson, A. T. C.; Drndić, M. In Situ Transmission Electron Microscopy Modulation of Transport in Graphene Nanoribbons. *ACS Nano* **2016**, *10*, 4004−4010.

(22) Parkin, W. M.; Balan, A.; Liang, L.; Das, P. M.; Lamparski, M.; Naylor, C. H.; Rodríguez-Manzo, J. A.; Johnson, A. T. C.; Meunier, V.; Drndić, M. Raman Shifts in Electron-Irradiated Monolayer MoS 2. *ACS Nano* **2016**, *10*, 4134−4142.

(23) Wang, H.; Luo, J.; Schäffel, F.; Rümmeli, M. H.; Briggs, G. A. D.; Warner, J. H. Carbon Nanotube Nanoelectronic Devices Compatible with Transmission Electron Microscopy. *Nanotechnology* **2011**, *22*, 245305.

(24) Peimyoo, N.; Yang, W.; Shang, J.; Shen, X.; Wang, Y.; Yu, T. Chemically Driven Tunable Light Emission of Charged and Neutral Excitons in Monolayer WS2. *ACS Nano* **2014**, *8*, 11320−11329.

(25) Zhu, B.; Chen, X.; Cui, X. Exciton Binding Energy of Monolayer WS2. *Sci. Rep.* **2015**, *5*, 9218.

(26) Zhao, W.; Ghorannevis, Z.; Amara, K.; Pang, J.; Toh, M.; Zhang, X.; Kloc, C.; Tan, P. H.; Eda, G. Lattice Dynamics in Mono-and Few-Layer Sheets of WS2 and WSe2. *Nanoscale* **2013**, *5*, 9677−9683.

(27) Loh, T. A. J.; Chua, D. H. C.; Wee, A. T. S. One-Step Synthesis of Few-Layer WS2 by Pulsed Laser Deposition. *Sci. Rep.* **2015**, *5*, 18116.

(28) Berkdemir, A.; Gutiérrez, H. R.; Botello-Méndez, A. R.; Perea-López, N.; Elías, A. L.; Chia, C.-I.; Wang, B.; Crespi, V. H.; López-Urías, F.; Charlier, J.-C.; Terrones, H.; Terrones, M. Identification of Individual and Few Layers of WS2 Using Raman Spectroscopy. *Sci. Rep.* **2013**, *3*, 1755.

(29) Ovchinnikov, D.; Allain, A.; Huang, Y.; Dumcenco, D.; Kis, A. Electrical Transport Properties of Single-Layer WS2. *ACS Nano* **2014**, *8*, 8174−8181.

(30) Khalil, H. M. W.; Khan, M. F.; Eom, J.; Noh, H. Highly Stable and Tunable Chemical Doping of Multilayer WS2 Field Effect Transistor: Reduction in Contact Resistance. *ACS Appl. Mater. Interfaces* **2015**, *7*, 23589−23596.

(31) Iqbal, M. W.; Iqbal, M. Z.; Khan, M. F.; Kamran, M. A.; Majid, A.; Alharbi, T.; Eom, J. Tailoring the Electrical and Photo-Electrical Properties of a WS2 Field Effect Transistor by Selective N-Type Chemical Doping. *RSC Adv.* **2016**, *6*, 24675−24682.

(32) Zhang, W.; Huang, J. K.; Chen, C. H.; Chang, Y. H.; Cheng, Y. J.; Li, L. J. High-Gain Phototransistors Based on a CVD MoS2 Monolayer. *Adv. Mater.* **2013**, *25*, 3456−3461.

(33) Perea-Lõpez, N.; Elías, A. L.; Berkdemir, A.; Castro-Beltran, A.; Gutiérrez, H. R.; Feng, S.; Lv, R.; Hayashi, T.; Lõpez-Urías, F.; Ghosh, S.; Muchharla, B.; Talapatra, S.; Terrones, H.; Terrones, M. Photosensor Device Based on Few-Layered WS2 Films. *Adv. Funct. Mater.* **2013**, *23*, 5511−5517.

(34) Garcia, A.; Raya, A. M.; Mariscal, M. M.; Esparza, R.; Herrera, M.; Molina, S. I.; Scavello, G.; Galindo, P. L.; Jose-Yacaman, M.; Ponce, A. Analysis of Electron Beam Damage of Exfoliated MoS2 Sheets and Quantitative HAADF-STEM Imaging. *Ultramicroscopy* **2014**, *146*, 33−38.

(35) Zan, R.; Ramasse, Q. M.; Jalil, R.; Georgiou, T.; Bangert, U.; Novoselov, K. S. Control of Radiation Damage in MoS2 by Graphene Encapsulation. *ACS Nano* **2013**, *7*, 10167−10174.

(36) Wang, S.; Lee, G.-D.; Lee, S.; Yoon, E.; Warner, J. H. Detailed Atomic Reconstruction of Extended Line Defects in Monolayer MoS2. *ACS Nano* **2016**, *10*, 5419−5430.

(37) Lui, C. H.; Frenzel, A. J.; Pilon, D. V.; Lee, Y. H.; Ling, X.; Akselrod, G. M.; Kong, J.; Gedik, N. Trion-Induced Negative Photoconductivity in Monolayer MoS2. *Phys. Rev. Lett.* **2014**, *113*, 166801.

(38) Yang, Y.; Peng, X.; Kim, H. S.; Kim, T.; Jeon, S.; Kang, H. K.; Choi, W.; Song, J.; Doh, Y. J.; Yu, D. Hot Carrier Trapping Induced

DOI: 10.1021/acsami.6b11480
ACS Appl. Mater. Interfaces 2016, 8, 32963−32970

Negative Photoconductance in InAs Nanowires toward Novel Nonvolatile Memory. *Nano Lett.* **2015**, *15*, 5875−5882.
(39) Nakanishi, H.; Bishop, K. J. M.; Kowalczyk, B.; Nitzan, A.; Weiss, E. A.; Tretiakov, K. V.; Apodaca, M. M.; Klajn, R.; Stoddart, J. F.; Grzybowski, B. A. Photoconductance and Inverse Photoconductance in Films of Functionalized Metal Nanoparticles. *Nature* **2009**, *460*, 371−375.
(40) Ratha, S.; Simbeck, A. J.; Late, D. J.; Nayak, S. K.; Rout, C. S. Negative Infrared Photocurrent Response in Layered WS2/reduced Graphene Oxide Hybrids. *Appl. Phys. Lett.* **2014**, *105*, 243502.
(41) Pandey, M.; Rasmussen, F. A.; Kuhar, K.; Olsen, T.; Jacobsen, K. W.; Thygesen, K. S. Defect-Tolerant Monolayer Transition Metal Dichalcogenides. *Nano Lett.* **2016**, *16*, 2234−2239.
(42) Yuan, S.; Roldán, R.; Katsnelson, M. I.; Guinea, F. Effect of Point Defects on the Optical and Transport Properties of MoS2 and WS2. *Phys. Rev. B: Condens. Matter Mater. Phys.* **2014**, *90*, 041402.
(43) Konstantatos, G.; Badioli, M.; Gaudreau, L.; Osmond, J.; Bernechea, M.; de Arquer, F. P. G.; Gatti, F.; Koppens, F. H. L. Hybrid Graphene−quantum Dot Phototransistors with Ultrahigh Gain. *Nat. Nanotechnol.* **2012**, *7*, 363−368.
(44) Lan, C.; Li, C.; Yin, Y.; Liu, Y. Large-Area Synthesis of Monolayer WS2 and Its Ambient-Sensitive Photo-Detecting Performance. *Nanoscale* **2015**, *7*, 5974−5980.
(45) Fan, Y.; Zhou, Y.; Wang, X.; Tan, H.; Rong, Y.; Warner, J. H. Photoinduced Schottky Barrier Lowering in 2D Monolayer WS 2 Photodetectors. *Adv. Opt. Mater.* **2016**, *4*, 1573−1581.
(46) Childres, I.; Jauregui, L. A.; Foxe, M.; Tian, J.; Jalilian, R.; Jovanovic, I.; Chen, Y. P. Effect of Electron-Beam Irradiation on Graphene Field Effect Devices. *Appl. Phys. Lett.* **2010**, *97*, 173109.
(47) Durand, C.; Zhang, X.; Fowlkes, J.; Najmaei, S.; Lou, J.; Li, A.-P. Defect-Mediated Transport and Electronic Irradiation Effect in Individual Domains of CVD-Grown Monolayer MoS2. *J. Vac. Sci. Technol. B, Nanotechnol. Microelectron. Mater. Process. Meas. Phenom.* **2015**, *33*, 02B110.
(48) Faruqi, A. R.; Henderson, R. Electronic Detectors for Electron Microscopy. *Curr. Opin. Struct. Biol.* **2007**, *17*, 549−555.

DOI: 10.1021/acsami.6b11480
ACS Appl. Mater. Interfaces 2016, 8, 32963−32970